Characterization and control of tunable quantum cascade laser beam parameters for stand-off spectroscopy

Robert Furstenberg*, Christopher A. Kendziora
Michael R. Papantonakis, Viet Nguyen and R. Andrew McGill
Naval Research Laboratory, 4555 Overlook Ave. SW, Washington, DC

ABSTRACT

Infrared active stand-off detection techniques often employ high power tunable quantum cascade lasers (QCLs) for target illumination. Due to the distances involved, any fluctuation of the laser beam direction and/or beam profile is amplified at the sample position. If not accounted for, this leads to diminished performance (both sensitivity and selectivity) of the detection technique as a direct result of uncertainties in laser irradiance at each imaged pixel of the sample. This is especially true for detection approaches which illuminate a relatively small footprint at the target since the laser beam profile spatial fluctuations are often comparable to the (focused) laser spot size. Also, there is often a necessary trade-off between high output QCL power and beam quality. Therefore, precise characterization of the laser beam profile and direction as a function of laser properties (tuning wavelength, current and operating mode: pulsed or CW) is imperative. We present detailed measurements of beam profiles, beam wander and power fluctuations and their reproducibility as function of laser wavelength and stand-off distance for a commercially available tunable quantum cascade laser. We present strategies for improving beam quality by compensating for fluctuations using a motorized mirror and a pair of motorized lenses. We also investigate QCL mode hops and how they affect laser beam properties at the sample. Detailed mode-hop stability maps were measured.

Keywords: Quantum cascade laser, QCL, beam parameters, beam profile, beam wander, mode hops, stand-off spectroscopy, photo-thermal spectroscopy

1. INTRODUCTION

We have been developing an eye-safe stand-off detection technique suitable for the detection of trace amounts of solid explosives (and other hazardous) particulates on solid surfaces[1-13]. In order to reach required detection sensitivity levels, we employ high-power (but below the eye-safe limit) tunable quantum cascade lasers (QCLs) as the active illumination source. Our detection platform uses a commercially available QCL system (MIRcat, Daylight Solutions Inc.)[14, 15]. Our technique (photo-thermal infrared imaging spectroscopy – PT-IRIS) involves shining an IR laser at the target and observing the small changes in thermal emissions. Due to the imaging nature of the technique, the distance to the target and the inhomogeneous distribution of analyte in a real-world target[16-18], it is essential to have good control over the pixel-level irradiance as raw spectra need to be ratioed by the power reaching each image pixel. Therefore, precise characterization of the laser beam profile and direction as a function of laser properties (tuning wavelength, current and operating mode: pulsed or CW) is imperative.

2. WAVELENGTH MEASUREMENT AND CALIBRATION

It was observed that the actual wavelength of the laser differs slightly from nominal values and a careful wavelength calibration is therefore needed. This was achieved by measuring the optical laser power by slowly tuning the laser through its tuning range by using the setup depicted in Figure 1a. The main purpose for using the integrating sphere was to increase the effective path length of the laser beam, which enhances absorption of weaker water vapor lines. Also, the integrating sphere reduces the laser power such that it does not saturate the sensitive HgCdTe (MCT) detector. The MCT

* Email: robert.furstenberg@nrl.navy.mil

Chemical, Biological, Radiological, Nuclear, and Explosives (CBRNE) Sensing XVII, edited by Augustus Way Fountain III,
Proc. of SPIE Vol. 9824, 98240L · © 2016 SPIE · CCC code: 0277-786X/16/$18 · doi: 10.1117/12.2224003

detector was used because of its fast response time (~1μs) and its ability to work in a dc-coupled configuration, needed for CW laser operation. The raw data showing the effect of water vapor absorption (Figure 1b) is processed into an absorbance-like quantity by dividing the raw spectrum with a fitted power envelope and taking the logarithm of the resulting spectrum. This was then compared to known water vapor spectra from the HITRAN[19] database. An algorithm is implemented that finds the optimal linear transformation of the measured spectra such that it fits the HITRAN database (in the least squares sense).

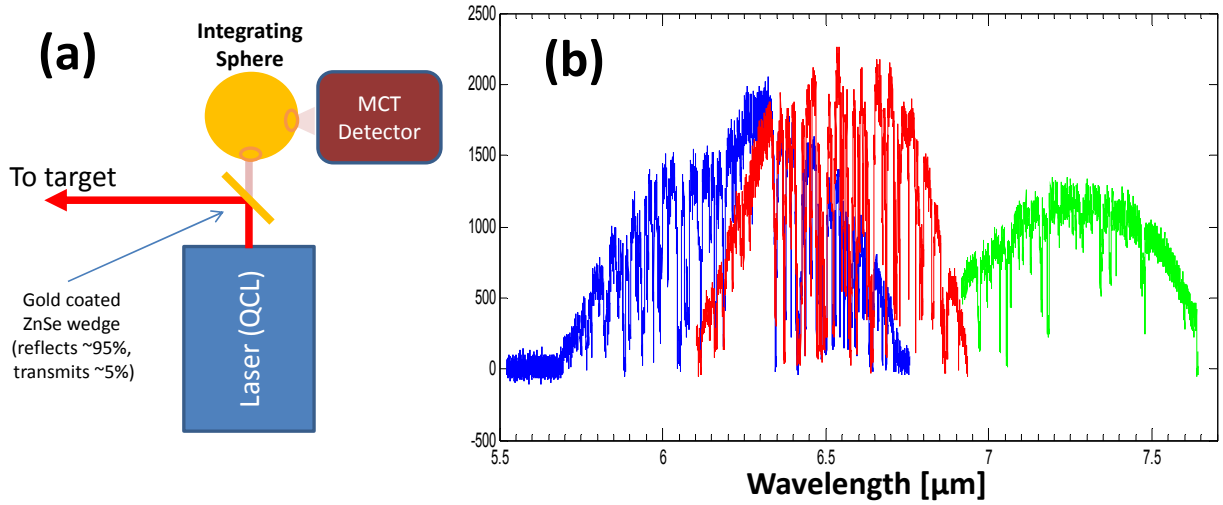

Figure 1. Experimental setup for wavelength measurement (a) and the raw data from the reference detector for 3 lasers showing atmospheric absorption lines (b).

The results of a typical wavelength calibration are shown in Figure 2. Figure 2a shows a section of the water vapor spectrum (based on the nominal QCL read-out) exhibiting a 13.8 nm wavelength shift with respect to HITRAN values. After wavelength calibration (Figure 2b), the peaks align with their corresponding HITRAN values. The high fidelity calibration is critical for the selection of wavelengths that can propagate through the atmosphere to the target, particularly in the spectral region between 5-8 μm, where the water vapor absorption lines are dense.

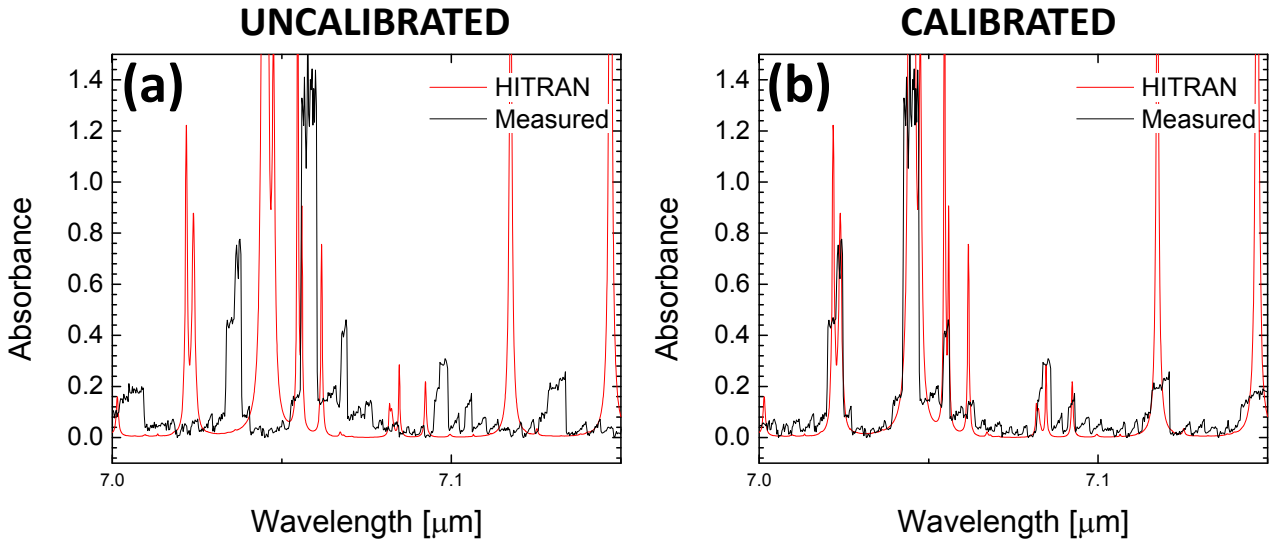

Figure 2. Section of the raw water vapor spectrum based on the nominal QCL read-out (a) showing the wavelength shift of 13.8 nm with respect to HITRAN values. After wavelength calibration (b), the peaks align with their corresponding HITRAN values.

3. LASER POWER MEASUREMENT AND CALIBRATION

For good spectra to be acquired, it is advisable to illuminate the sample with a uniform power across the whole spectral range. Since QCLs are laser diodes, we adjust the laser drive current to achieve a certain power output. To do this, we first collect I-P curves at each wavelength in the spectrum and use this to generate a look-up table used to determine the optimal drive current for a selected power. Figure 3 shows current-power (I-P) curves for two QCL wavelengths. A good laser wavelength (as shown in Figure 3a) has a near-linear I-P curve, while a wavelength prone to mode-hopping close to an absorption feature (as shown in Figure 3a) exhibits a complex I-P curve due to the large difference in attenuation between the two laser modes.

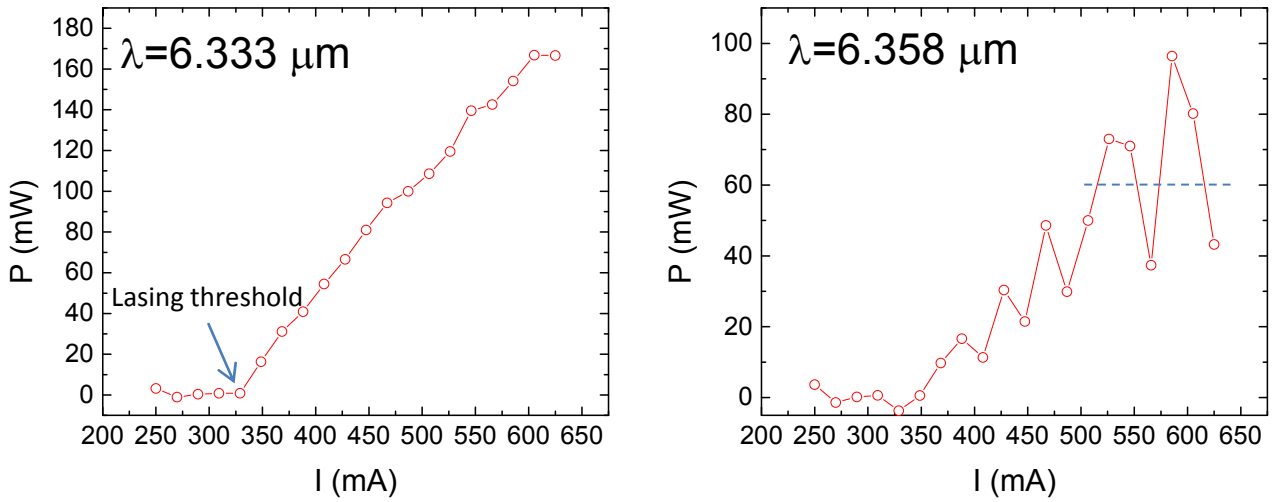

Figure 3. Current-power (I-P) curves for two QCL wavelengths. A good laser wavelength will have near-linear I-P curve (left), while a line close to an absorption feature will exhibit a complex I-P curve (with multiple current values producing the same optical power, as indicated by the blue dashed line) due to mode-hopping (right).

For stand-off spectroscopy, it is not enough to just measure the power near the exit port of the laser (as was done above), and therefore, the power needs to be measured (or calculated) at the sample. The reason for this lies in the fact that laser lines outside the atmospheric transmission windows (3-5 μm and 8-12 μm) can experience attenuation on the way to the sample due to being close to water vapor lines. Knowing the precise wavelength of the laser would, in principle, allow for the calculation of the power attenuation (using absorbance values from HITRAN database and measured relative humidity values), however, this is not feasible for the MIRcat QCL system due to strong mode-hopping.

To solve this problem, we employ two reference detectors for the dynamic (i.e. time-resolved) measurement of absorbance. The experimental setup for this measurement is given in Figure 4 below.

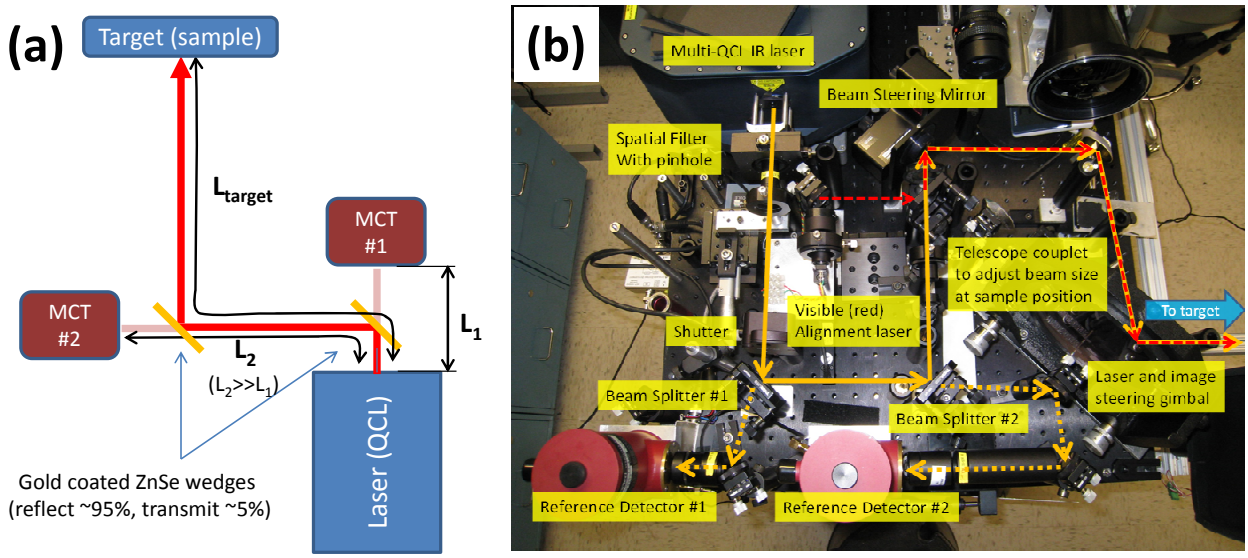

Figure 4. Schematic drawing (a) and photograph of the NRL PT-IRIS stand-off detection platform (b) for measuring the absorbance using two reference detectors. The absorbance value is used to predict the laser power reaching the sample.

A small fraction of the laser beam is picked-off at two points along the optical path and directed to two MCT detectors. One of the detectors is placed as close to the laser exit port as possible (at distance L_1), while the other is placed as far away as possible (using fold mirrors), at a distance L_2. This way, we can measure the laser beam attenuation along the known distance (L_2 -L_1):

$$P_1 = V_1\Re_1 = P_0 e^{-\alpha L_1}$$
$$\Rightarrow \quad \alpha = \frac{\ln\left(V_1\Re_1 / V_2\Re_2\right)}{L_2 - L_1} \tag{1}$$
$$P_2 = V_2\Re_2 = P_0 e^{-\alpha L_2}$$

Once we know the absorbance, we can predict the attenuation at the target (assuming we know the distance to the target, L_{target}):

$$P_{\text{target}} = P_0 e^{-\alpha L_{target}} \quad \Rightarrow \quad P_{\text{target}} = V_2\Re_2\left(\frac{V_1\Re_1}{V_2\Re_2}\right)^{\frac{L_2 - L_{\text{target}}}{L_2 - L_1}} \tag{2}$$

The responsivity factors $\Re_1$ and $\Re_2$ combine the detector responsivities and the losses at various optics. $\Re_1$ and $\Re_2$ are weak functions of the wavelength and can be determined prior to this procedure and stored in a look-up table.

To properly implement the two-detector method we decided against using integrating spheres because the effective path length of the integrating sphere is *a priori* unknown and needs to be measured. Furthermore, this effective path length can be shown to be absorbance dependent, which would preclude the use of the simple formula given in Equation 1, and would require an iterative approach. However, without integrating spheres, the pronounced beam wander of the laser (*vide infra*) makes this method unreliable. To remedy this, we place a weakly pressed KBr pellet before the detectors to induce diffuse scattering.

4. BEAM SIZE AND POINTING MEASUREMENT AND CALIBRATION

The beam profile and beam position are measured either by a commercial beam profiler (e.g. Pyrocam III by Ophir/Spiricon) or by the IR camera in the stand-off detection system (by observing laser backscatter off a roughened surface or photo-thermal differential images of a low-thermal diffusivity surface). Measured beam profiles (using calibrated camera pixels) are subsequently fitted (using the conjugate-gradient optimization method) to a general bivariate normal distribution[20] given by the following expression for the laser irradiance:

$$I(x,y) = \frac{P_0}{2\pi\sigma_x\sigma_x\sqrt{1-r^2}} \exp\left(-\frac{1}{2(1-r^2)} \left[\frac{(x-\mu_x)^2}{\sigma_x^2} + \frac{(y-\mu_y)^2}{\sigma_y^2} - \frac{2r(x-\mu_x)(y-\mu_y)}{\sigma_x\sigma_y} \right] \right) \quad (3)$$

An example of a typical fitting result is shown in Figure 5. Also shown is the difference between fit and measurement that represents the deviation of the QCL beam form a perfect Gaussian beam profile.

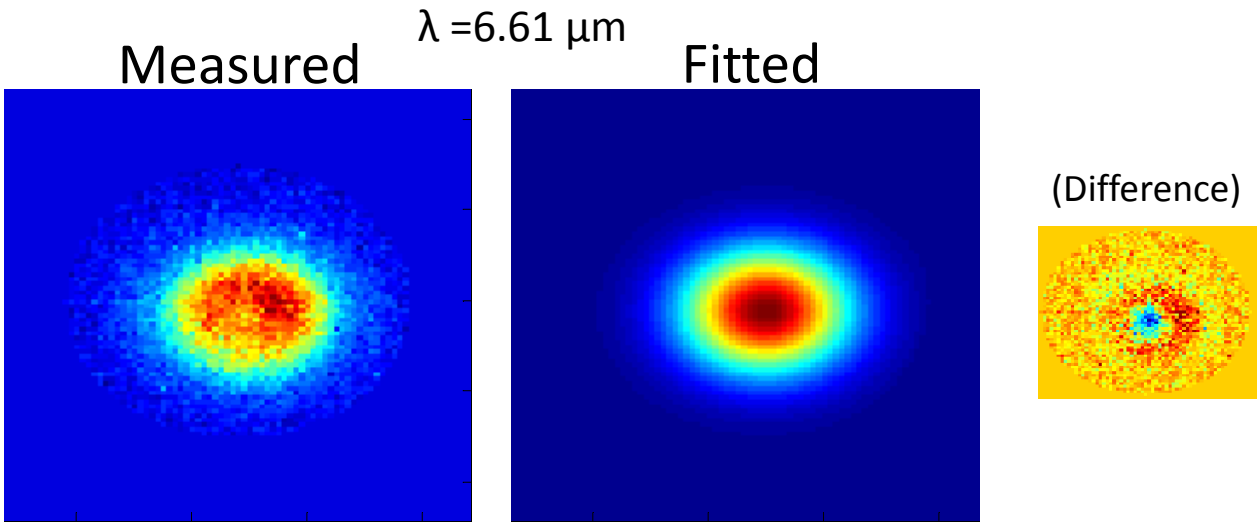

Figure 5. Measured (using photo-thermal method) and fitted (using 2D elliptical Gaussian) beam profiles of the QCL beam (λ=6.61 μm). Also shown is the difference between fit and measurement that represents the deviation of the QCL beam from a perfect Gaussian beam profile.

To evaluate beam pointing stability, we measure the beam profiles across the tuning range of each of the 4 QCLs in the MIRcat module. The beam position (*x* and *y* coordinate of the beam centroid) and average size of the beam are shown in Figure 6 and Figure 7 for CW and pulsed operation, respectively. The beam pointing pattern between the CW and pulsed operation mode is different but the overall magnitude of the fluctuations is similar.

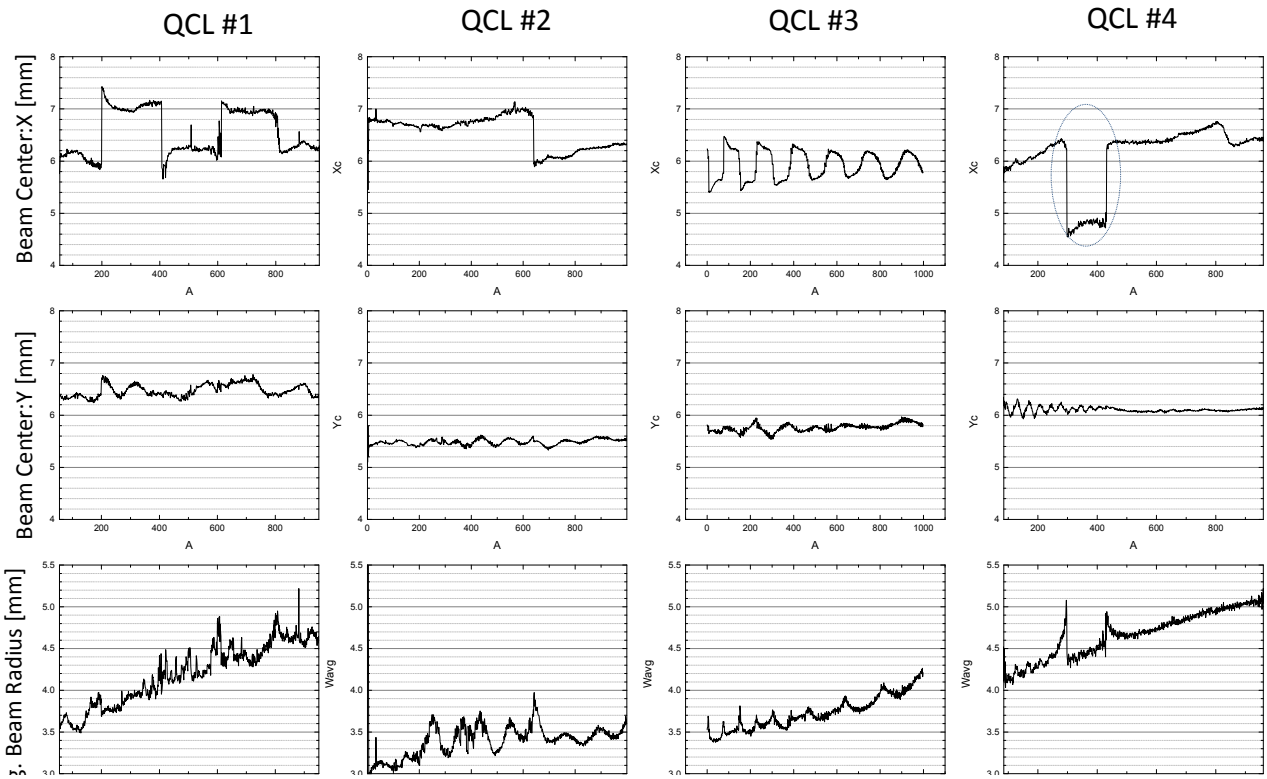

Figure 6. Beam profile parameters at a 1 meter stand-off for the 4 QCL chips in the MIRcat module across their respective tuning ranges operated in the CW mode. X coordinate (top panels) , Y coordinates (middle panels) and average beam size (bottom) panel are shown. The X centroid position fluctuates ~2.5 mrad (1mm=1mrad).

Since the extent of fluctuations in beam position (centroid) and beam size is too large to be suitable for stand-off spectroscopy, we modified the beam using a combination of a motorized mirror (to compensate for beam direction fluctuations) and a pair of lenses (one motorized, one fixed) to compensate for beam size fluctuation, as shown in Figure **8**. A beam position calibration procedure consists of measuring the beam profile parameters (beam centroid and size) as a function of the motorized lens position (going in and out of focus, as shown on right in Figure 8), at a few select stand-off distances. This information is then saved in a look-up table. A large part of the beam position (centroid) and beam size fluctuations are reproducible.

To demonstrate the beam position calibration, we recorded the beam profile (without any correction) for a series of 68 wavelengths (spanning the whole tuning range of the MIRcat QCL system, as shown in Video 1 (left). Video 2 (right) shows the same beam profile sequence with the beam position calibration applied. The beam profile parameters (centroid and size) for these videos are shown in Figure 9.

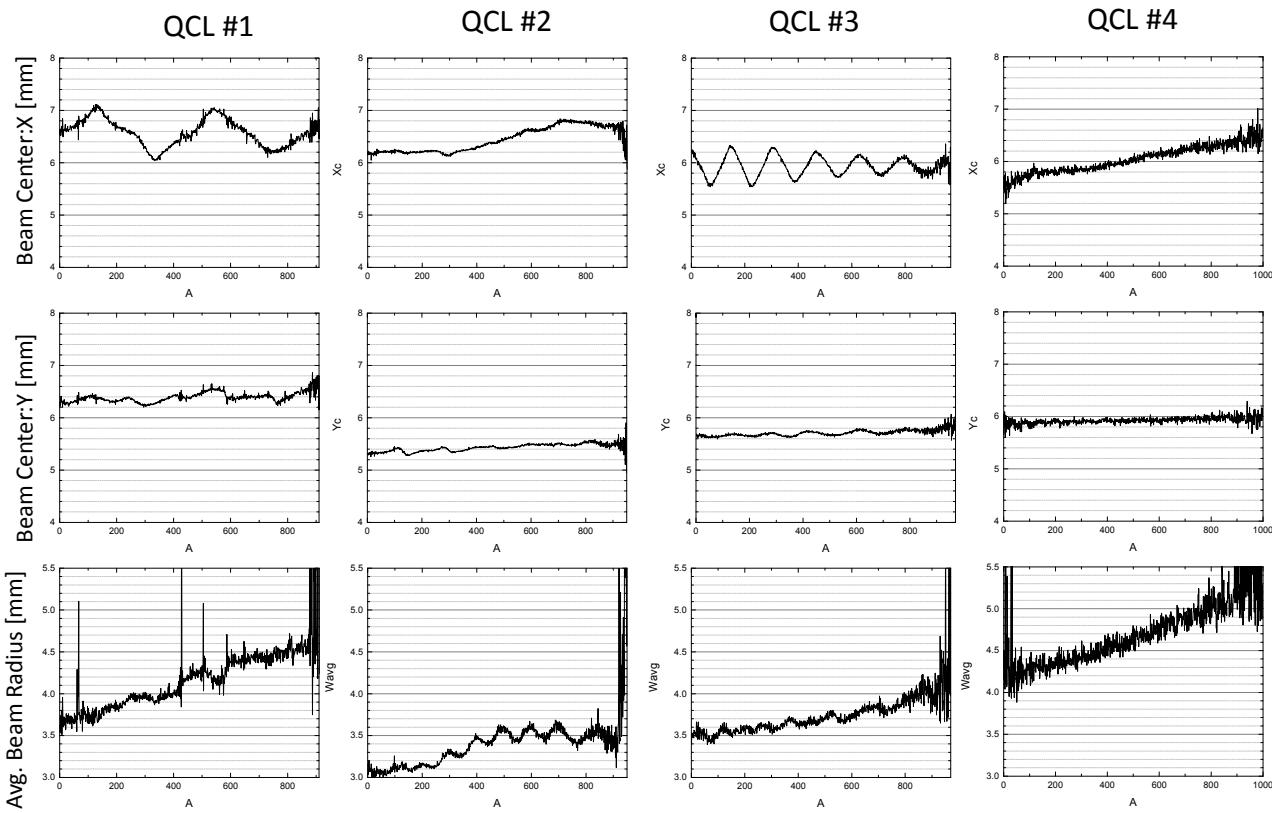

Figure 7 Beam profile parameters at a 1 meter stand-off for the 4 QCL chips in the MIRcat module across their respective tuning ranges operated in the pulsed mode. X coordinate (top panels) , Y coordinates (middle panels) and average beam size (bottom) panel are shown. The X centroid position fluctuates ~2 mrad (1mm=1mrad).

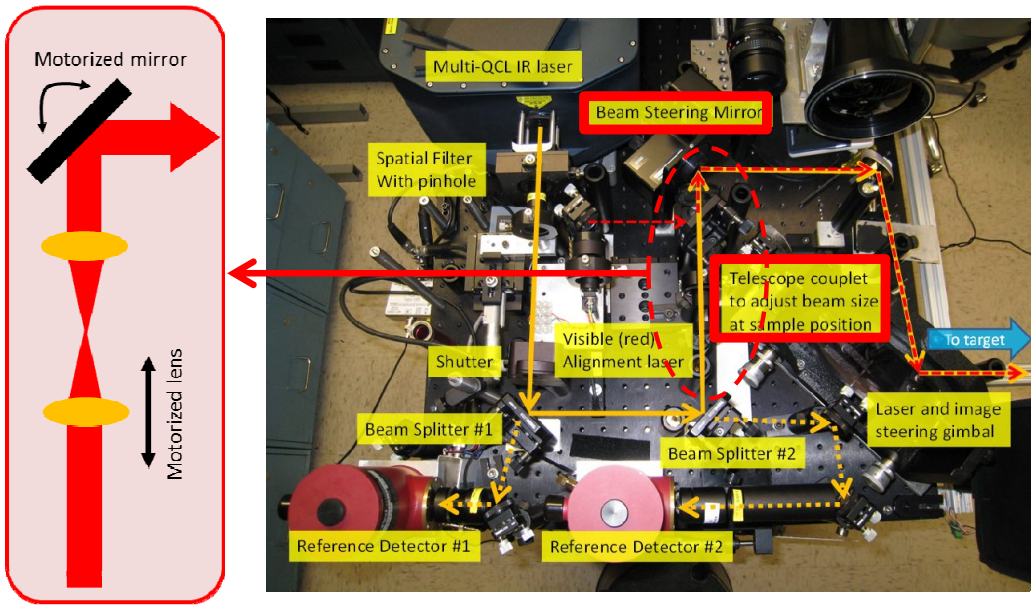

Figure 8. The laser beam calibration and beam shaping setup (right) and schematic drawing (left) of the beam shaping unit consisting of a pair of motorized lenses and a motorized mirror.

UNCORRECTED

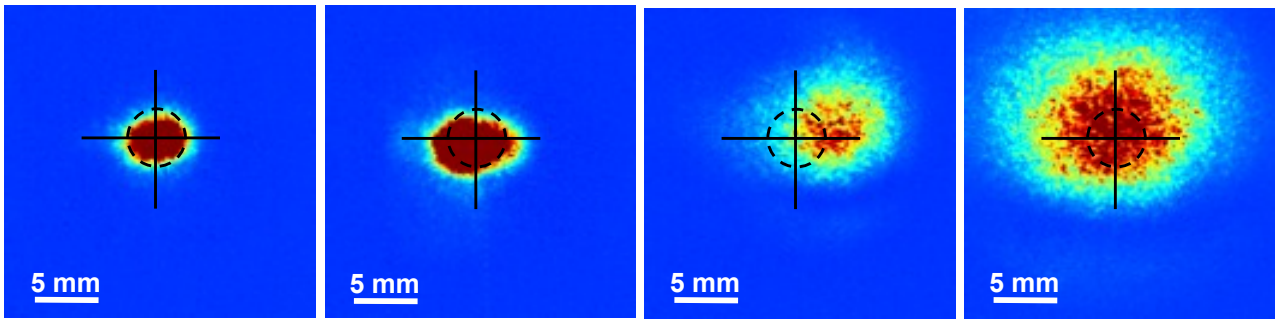

λ=6.17 µm λ=6.92 µm λ=9.0 µm λ=10.4 µm

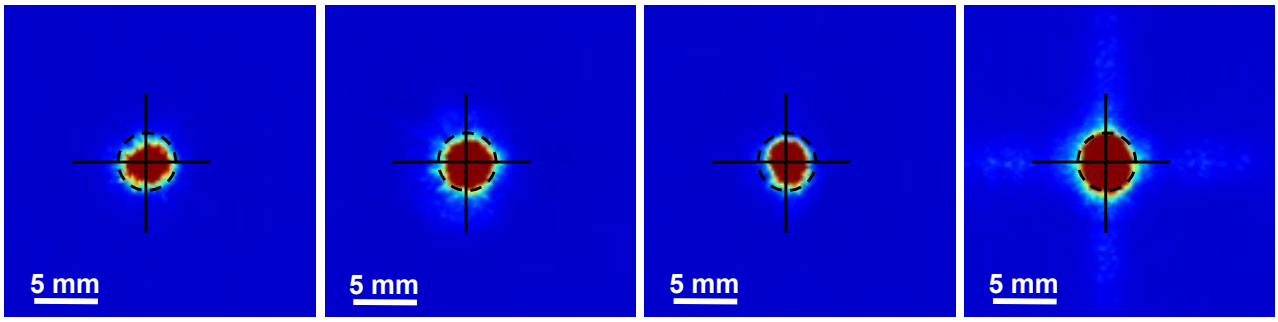

CORRECTED for beam wander & size change

Video 1 (top). Uncorrected beam profiles of the MIRcat QCL tuned through 68 wavelengths in the 6-11 µm range. The beam profiles were recorded at 1 meter. Only 4 wavelengths show, for full video click here: http://dx.doi.org/10.1117/12.2224003.1

Video 2 (bottom).Corrected beam profiles of the MIRcat QCL tuned through 68 wavelengths in the 6-11 µm range. The beam profiles were recorded at 1 meter. Only 4 wavelengths show, for full video click here: http://dx.doi.org/10.1117/12.2224003.2

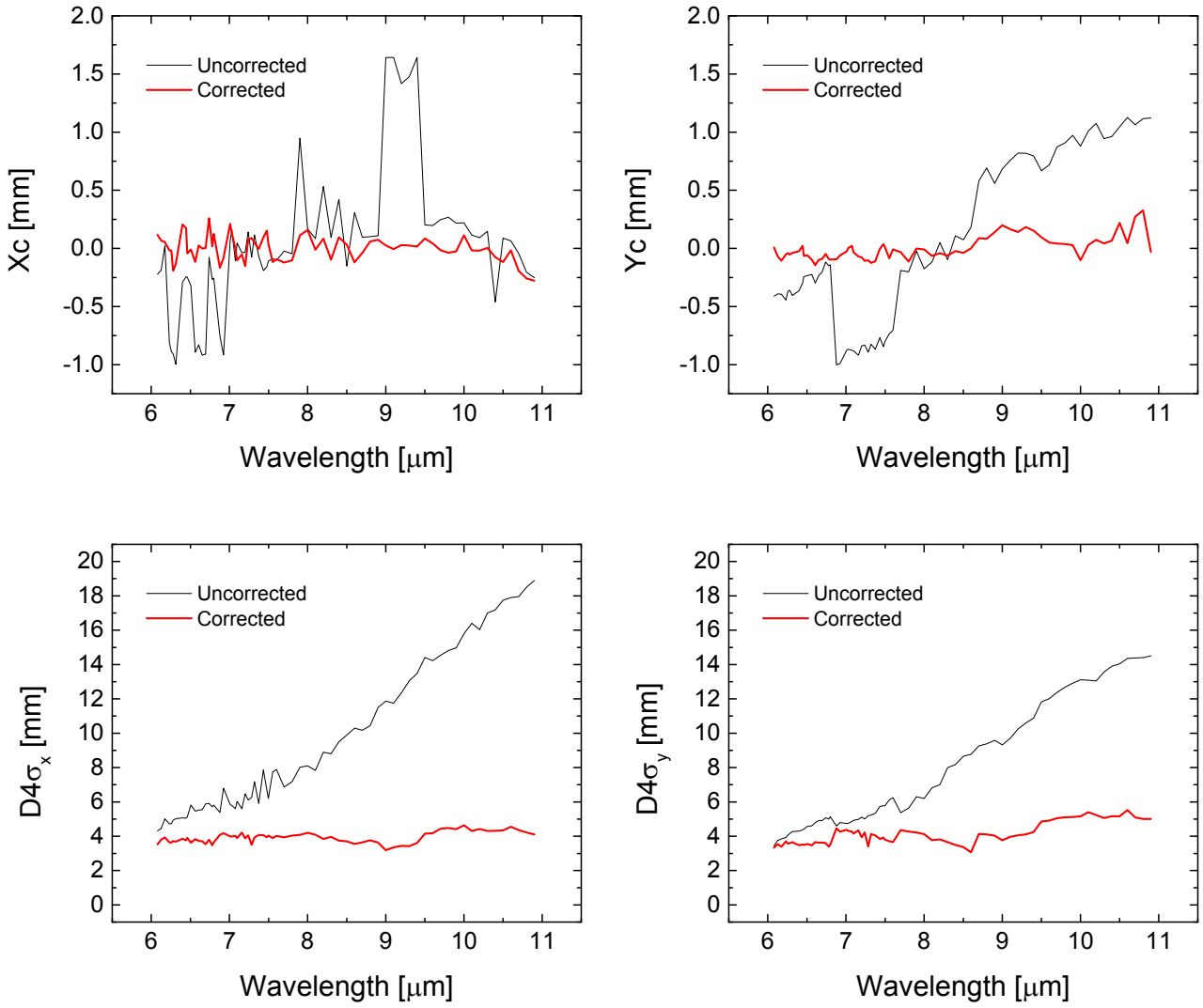

Figure 9. Beam centroids (top panels) and beam size (bottom panels) with beam size and position correction (red curve) and without (black curve) for the beam profiles shown in Videos 1 and 2.

5. QCL MODE HOP ANALYSIS

QCLs can exhibit wavelength instability due to longitudinal and/or transverse mode hops. A mode hop usually manifests itself as a sudden shift in output wavelength accompanied with a laser power shift as well as a slight change in laser propagation direction. Near water vapor lines, this is especially problematic as a very slight change in wavelength can cause a large change in laser power at the sample due to large differences in air absorbance between the two modes. The time difference between two mode hops varies from <1ms to many seconds. A typical oscilloscope trace of the reference detector showing mode-hop induced power fluctuations is shown in Figure 10. To quantify the intensity (and number) of modes hopes in a given oscilloscope trace, we calculate the fast Fourier transform (FFT) of the trace and report the FFT intensity at the highest frequency which correlates well with the magnitude of the voltage jump, as shown in Figure 11.

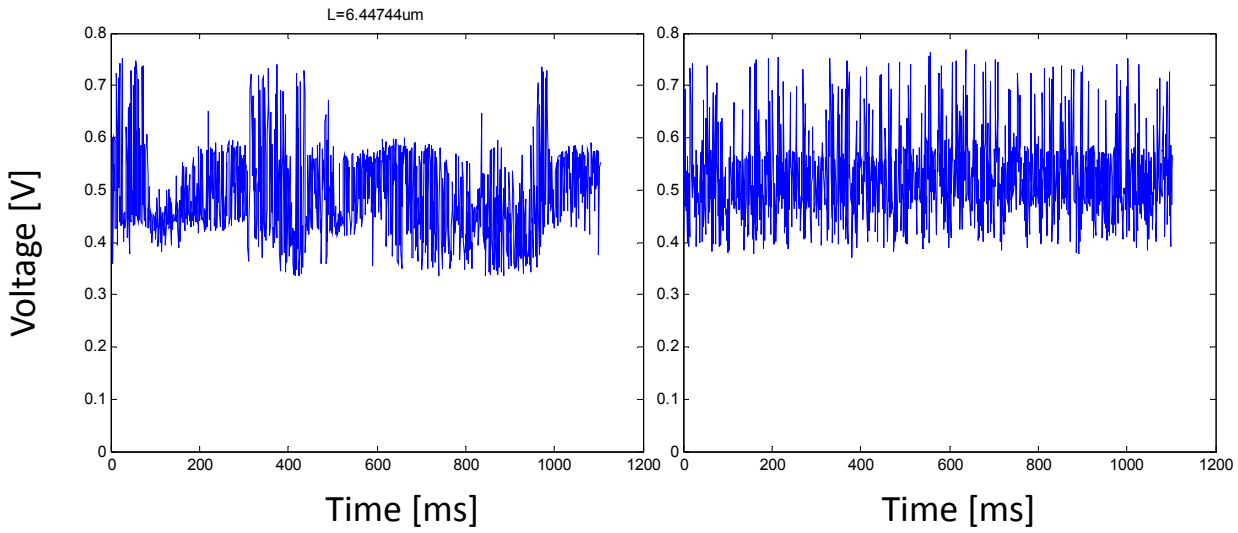

Figure 10. Typical oscilloscope traces of the reference detector showing mode-hop induced power fluctuations.

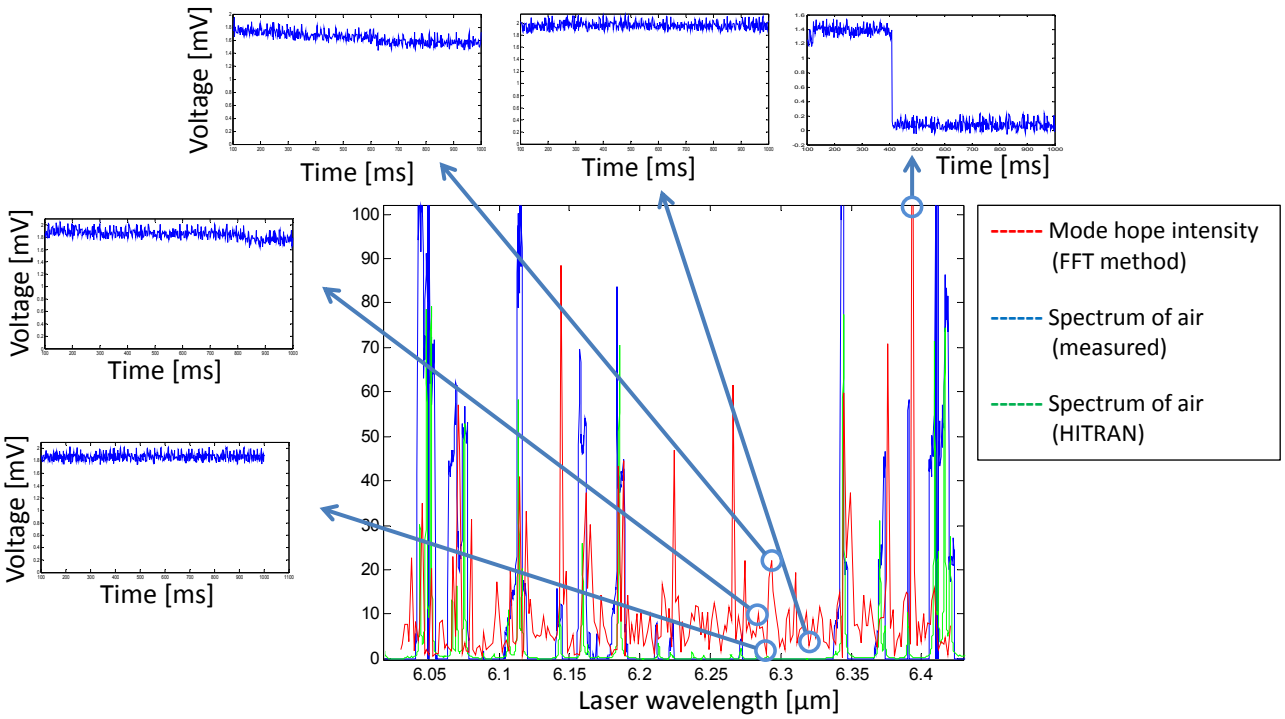

Figure 11. Mode-hop jump intensity plot (red curve) based on the maximum FFT frequency method for a number of laser wavelengths in the ~6 to ~6.5 μm range. For several points of the red curve, the corresponding oscilloscope traces illustrate that the severity of mode-hopes correlates with the maximum frequency FFT value. The green and blue curves correspond to HITRAN and measured air absorption, respectively.

Another useful metric for quantifying mode-hops is the Anderson-Darling (AD) score[21], which is a statistical test used to determine the similarity between an unknown distribution and the normal distribution. In our case, the distribution is obtained by constructing a histogram of the reference detector voltages. Traces with mode hops will exhibit a

multimodal (non-normal) distribution and will have a higher AD score. A mode-hop free trace would only exhibit white noise which is normally distributed around some mean value, which would produce a low AD score.

Figure 12 shows the AD score for a large number of laser operating points (i.e. wavelength-current combinations) for the first three QCLs in the MIRcat system. We refer to this figure as the "stability map". Blue points have low AD score while red points have high AD score. The mode hops are clearly more severe in regions where the water absorption is strong. At each wavelength, as the current is increased, there are regions where mode-hops are less severe ("islands of stability" – blue regions in the image). To minimize mode hops, one needs to select wavelength-current combinations from the stability map with low AD scores.

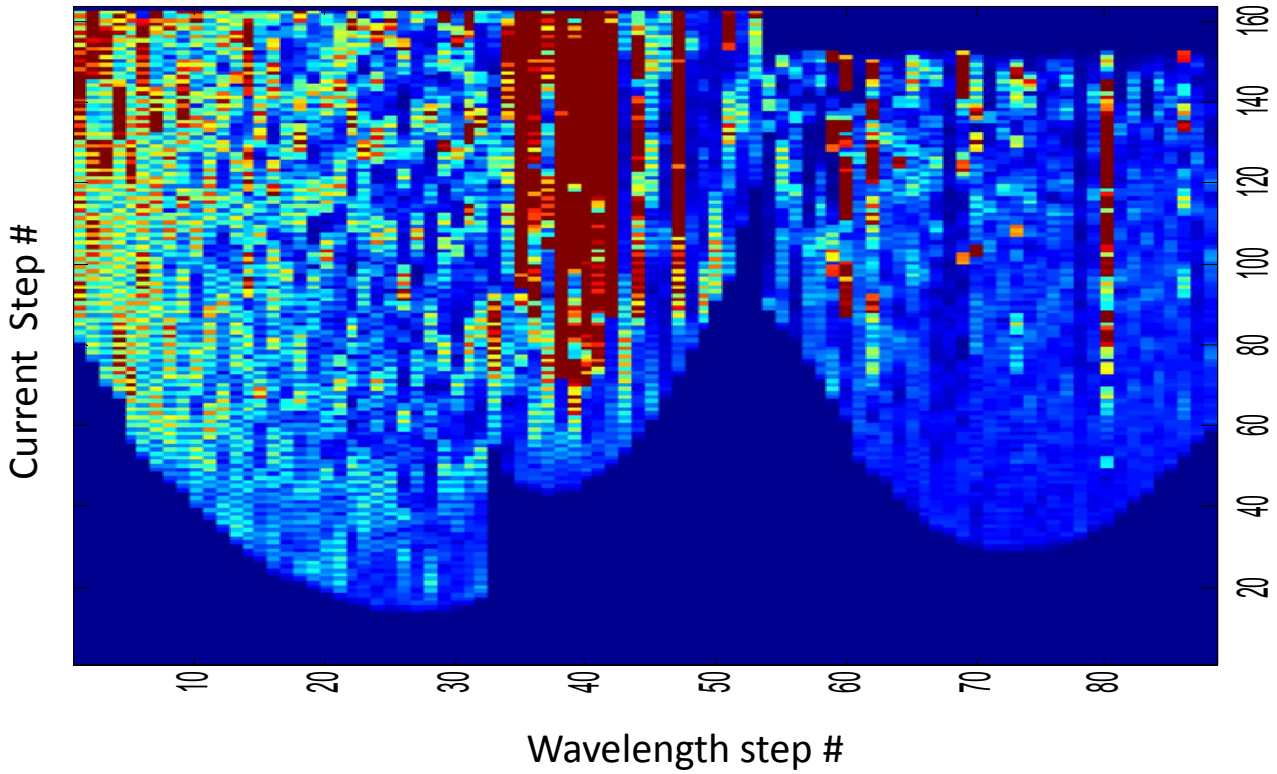

Figure 12. The stability map showing the AD score for a number of wavelength-current laser operating points for the first three QCLs in the MIRcat system. The AD score was calculated from a 2 second trace at each operating point. At each wavelength, as the current is increased, there are regions where mode-hops are less severe ("islands of stability"). To minimize mode hops, one needs to select wavelength-current combinations from the stability map with low AD scores.

6. CONCLUSIONS

Laser requirements for stand-off detection are more stringent than for other applications, therefore, existing commercial "turn-key" QCL systems cannot be used for stand-off spectroscopy without careful calibration and monitoring of the laser parameters. We presented several methods for the calibration of wavelength, power and beam size and profile and demonstrated the improvement in laser beam pointing stability.
We have also presented a novel characterization method for assessing mode-hops in QCLs.

REFERENCES

[1] Furstenberg, R., Kendziora, C., Stepnowski, J. *et al.*, "Stand-off detection of trace explosives via resonant infrared photothermal imaging," Appl. Phys. Lett., 93(22), (2008).

[2] Kendziora, C., Furstenberg, R., Papantonakis, M. *et al.*, "Advances in stand-off detection of trace explosives by infrared photo-thermal imaging," Proc. SPIE, 7664, 76641J (2010).

[3] Furstenberg, R., Kendziora, C., Papantonakis, M. *et al.*, "Stand-off detection of trace explosives by infrared photo-thermal spectroscopy," 2009 IEEE Conference on Technologies for Homeland Security (HST), 465-71 (2009).

[4] Papantonakis, M., Kendziora, C., Furstenberg, R. *et al.*, "Stand-off detection of trace explosives by infrared photothermal imaging," Proc. SPIE, 7304, 730418 (2009).

[5] Kendziora, C. A., Jones, R. M., Furstenberg, R. *et al.*, "Infrared photothermal imaging for standoff detection applications," Proc. SPIE, 8373, 83732H (2012).

[6] Furstenberg, R., Grosser, J., Kendziora, C. A. *et al.*, "Modeling of the Laser-Analyte-Substrate Interaction in Photo-thermal Infrared Imaging and Laser Trace Vaporization," Proc. SPIE, 8013, 801318 (2011).

[7] Kendziora, C. A., Furstenberg, R., Jones, R. M. *et al.*, "Remote Explosives Detection (RED) by Infrared Photothermal Imaging," 2011 Fall Materials Research Society Meeting, 1405, (2011).

[8] Furstenberg, R., Kendziora, C. A., Papantonakis, M. R. *et al.*, "Chemical Imaging using Infrared Photo-thermal Microspectroscopy," Proc. SPIE, 8374, 837411 (2012).

[9] Kendziora, C. A., Furstenberg, R., Jones, R. M. *et al.*, "Remote Explosives Detection (RED) by Infrared Photothermal Imaging," MRS Proceedings Fall 2011, 1405, (2012).

[10] Furstenberg, R., Kendziora, C., Papantonakis, M. *et al.*, "Advances in photo-thermal infrared imaging microspectroscopy," Proc. SPIE, 8729, 87290H (2013).

[11] Kendziora, C. A., Furstenberg, R., Papantonakis, M. *et al.*, "Infrared photothermal imaging of trace explosives on relevant substrates," Proc. SPIE, 8709, 87090O (2013).

[12] Kendziora, C. A., Furstenberg, R., Papantonakis, M. *et al.*, "Detection of trace explosives on relevant substrates using a mobile platform for photothermal infrared imaging spectroscopy (PT-IRIS)," Proc. SPIE, 9467, 94672R (2015).

[13] Furstenberg, R., Kendziora, C. A., Papantonakis, M. R. *et al.*, "Trace explosives detection using photo-thermal infrared imaging spectroscopy (PT-IRIS): theory, modeling, and detection algorithms," Proc. SPIE, 9455, 94550I (2015).

[14] Day, T., Pushkarsky, M., Caffey, D. *et al.*, "Quantum cascade lasers for defense and security," Proc. SPIE, 8898, 889802 (2013).

[15] Day, T., Takeuchi, E. B., Weida, M. *et al.*, "High-power lightweight external-cavity quantum cascade lasers," Proc. SPIE, 7325, 73250J (2009).

[16] Nguyen, V., Furstenberg, R., Carr, N. *et al.*, "Fate and effects of trace particulate explosives," Proc. SPIE, 9073, 90730R (2014).

[17] Furstenberg, R., Nguyen, V., Fischer, T. *et al.*, "Advances in sublimation studies for particles of explosives," Proc. SPIE, 9455, 94550R (2015).

[18] Nguyen, V., Papantonakis, M., Furstenberg, R. *et al.*, "'Real World' Particulate Explosives Test Coupons for Optical Detection Applications," Proc. SPIE, 8710, 87100T (2013).

[19] Rothman, L. S., Gordon, I. E., Babikov, Y. *et al.*, "The HITRAN2012 molecular spectroscopic database," Journal of Quantitative Spectroscopy & Radiative Transfer, 130, 4-50 (2013).

[20] Bertsekas, D. P., and Tsitsiklis, J. N., [Introduction to Probability], Athena Scientific, Belmont, Massachusetts (2002).

[21] Anderson, T. W., and Darling, D. A., "Asymptotic Theory of Certain 'Goodness of Fit' Criteria Based on Stochastic Processes," Annals of Mathematical Statistics, 23(2), 193-212 (1952).